

# Coexistence of Single and Double-Quantum Vortex Lines

Ü. Parts<sup>a</sup>, V.V. Avilov<sup>b</sup>, J.H. Koivuniemi<sup>a</sup>, N.B. Kopnin<sup>a,c</sup>, M. Krusius<sup>a</sup>, J.J. Ruohio<sup>a</sup>, and V.M.H. Ruutu<sup>a</sup>

<sup>a</sup>Low Temperature Laboratory, Helsinki University of Technology, P.O.Box 2200, FIN-02015 HUT, Finland

<sup>b</sup>Department of Magnetohydrodynamics, Research Center Rossendorf, P.O.Box 510119, D-01314 Dresden, Germany

<sup>c</sup>L. D. Landau Institute for Theoretical Physics, 117334 Moscow, Russia

(August 11, 2018)

We discuss the configurations in which singly and doubly quantized vortex lines may coexist in a rotating superfluid. General principles of energy minimization lead to the conclusion that in equilibrium the two vortex species segregate within a cylindrical vortex cluster in two coaxial domains where the singly quantized lines are in the outer annular region. This is confirmed with simulation calculations on discrete vortex lines. Experimentally the coexistence can be studied in rotating superfluid <sup>3</sup>He-A. With cw NMR techniques we find the radial distribution of the two vortex species to depend on how the cluster is prepared: (i) By cooling through  $T_c$  in rotation, coexistence in the minimum energy configuration is confirmed. (ii) A glassy agglomerate is formed if one starts with an equilibrium cluster of single-quantum vortex lines and adds to it sequentially double-quantum lines, by increasing the rotation velocity in the superfluid state. This proves that the energy barriers, which separate different cluster configurations, are too high for metastabilities to anneal.

PACS: 67.57.Fg, 52.25.Wz, 74.60.Ge

## I. INTRODUCTION

Superfluid <sup>3</sup>He-A is the only known quantum system where topologically stable vortex lines with different quantization appear simultaneously. The doubly quantized vortex (DQV) is formed at low critical velocity and is usually obtained when superfluid <sup>3</sup>He-A is accelerated to motion, eg. in a rotating container [1]. The singly quantized vortex (SQV), in turn, may have lower energy, depending on the magnitude of the magnetic field and flow velocity, but because of its large critical velocity it is in practice only formed on cooling through the superfluid transition in nonzero flow [2].

Normally one will find either double or single-quantum vortex lines in a rotating container, depending on how the state has been prepared. In the homogeneous rotating superfluid, transitions between different vortex textures are of first order and therefore in principle sharp. However, topological stability forbids a transition from one type of existing vortex lines to another. Thus SQV and DQV lines, once they have been formed, will maintain their quantization in the rotating container, as long as they are not removed by deceleration and annihilation on the container wall or by warming up to the normal phase. This metastability can be exploited to prepare a rotating state where both types of vortex lines are simultaneously present.

*A priori* it is not clear what configuration a rotating state with two different vortex species would take: Do the arrays always have the same configuration or does this depend on the process by which the state has been created? Similar questions have been studied in the case of point-like objects, namely trapped ions in a 2 or 3-dimensional point charge system [3]. We investigate the coexistence of SQV and DQV lines both theoretically and

experimentally. We study the free energies of different vortex-array configurations, which consist of a mixture of the two species or of segregated domains. We apply both the continuum model and use numerical simulation of discrete vortex lines to show that a configuration with SQV vortices surrounding an inner central cluster of DQV is lower in energy than any other configuration. The energy difference is small and disappears in the continuum approximation.

Axially symmetric configurations of coexisting SQV and DQV lines are observed in our measurements when liquid <sup>3</sup>He is slowly cooled at constant rotation from the normal phase to <sup>3</sup>He-A. Our observations of these states agree with the theoretical predictions: the SQV lines are found in an outer annulus which surrounds a central domain of DQV lines. Segregated configurations, which do not have full axial rotation symmetry, can also be prepared. This is accomplished by adding DQV lines to an existing equilibrium SQV cluster, by slowly increasing the rotation velocity at constant temperature in the superfluid state. The resulting configuration does not correspond to the global energy minimum, but rather resembles a glassy agglomerate.

## II. ROTATING <sup>3</sup>HE-A.

Rotating vortex states are driven and stabilized by superfluid counterflow (CF), the difference in the velocities of the normal and superfluid fractions,  $\mathbf{v} = \mathbf{v}_n - \mathbf{v}_s$ . The equilibrium states are found by minimizing the free energy functional [4], which controls the spatial distribution of the order parameter. On the macroscopic scale, vortex textures in <sup>3</sup>He-A are rectilinear structures, oriented parallel to the rotation axis, which extend from the top

to the bottom of the rotating container. These vortex cells are confined by the Magnus force to a regular array, a cluster of vortex lines. The cluster is coaxial with the cylinder [9] and isolated from the cylindrical wall by an annular layer of vortex-free CF. Within the cluster the areal density of linear vortex cells has the solid-body-rotation value  $n = 2\Omega/\kappa$ . Here  $\kappa = \nu\kappa_0$  is the circulation of a vortex line with the quantum number  $\nu$  and the circulation quantum  $\kappa_0 = h/(2m_3) = 0.066 \text{ mm}^2/\text{s}$ .

In a vortex cluster of infinite diameter a transverse cross section would display a perfect 2-dimensional lattice with triangular nearest-neighbor coordination, which arises from the inter-vortex repulsion. In a finite cluster the central region is expected to display a triangular lattice, which approaches crystalline order, but towards the outer boundary it is deformed by the surrounding annular CF more and more towards a configuration of concentric rings of vortex lines [10]. Due to the competition between volume and surface interactions long range order is thus relatively poor in finite-size arrays at the usual experimentally accessible rotation velocities. Here the total number of lines is typically a few hundred, the radius  $R$  of the container a few mm, the radius of the Wigner-Seitz (WZ) cell of the vortex lattice  $r_0 \sim 100 \mu\text{m}$ , and the vortex core radius  $\xi \sim 10 \mu\text{m}$  [11].

The order-parameter texture within a unit cell of the periodic vortex lattice has been derived from numerical minimization of the free energy as a function of the rotation velocity  $\Omega$  and the applied field  $\mathbf{H}$  [5,2,6]. These calculations reveal a complex phase diagram [2,6], with quantized vorticity organized in several topologically and structurally different vortex textures [7]. SQV vortex textures, which include a singular vortex core, have only been described approximately, by solving for the order parameter distribution with analytical trial functions [8]. Of these different vortex textures we shall here only be concerned with two, the continuous DQV and the singular SQV.

In an array consisting of DQV lines the inter-vortex distance is larger by  $\sqrt{2}$  than in one formed from SQV lines. With coexisting SQV and DQV lines this large difference opens the question whether sufficient mismatch and distortion is created in the nearest-neighbor coordination that a disordered glassy state results. Or could it perhaps lead to a ‘‘chemical’’ structure where both species occupy fixed positions within each unit cell of a periodic vortex lattice. A third possibility is an array consisting of segregated domains of one species only. These are the questions which we shall discuss next.

### III. ENERGY MINIMIZATION

#### A. Continuum approximation

On the macroscopic level the energy difference between SQV and DQV arrays depends on the difference in the quantization numbers and inter-vortex distances, if the latter are much larger than the core sizes. Here we neglect the smaller energy contributions associated with the structure of the vortex core. Consider the free energy of the rotating superfluid

$$\tilde{E}\{\mathbf{v}_s\} = E_{kin} - L\Omega = \frac{\rho_s}{2} \int_{r < R} (\mathbf{v}_s^2 - 2\mathbf{v}_s \mathbf{v}_{rot}) d^2r, \quad (1)$$

where  $\mathbf{v}_{rot} = \Omega[\hat{\mathbf{z}} \times \mathbf{r}]$ ,  $\Omega$  is the rotation velocity, and  $L$  the angular momentum of the fluid. We express the superflow velocity  $\mathbf{v}_s$  in the continuum approximation and assume the logarithmic approximation for the vortex line energy. In the laboratory frame we then have [12]

$$\tilde{E} = \frac{\rho_s}{2} \int \left[ v_s^2 + \frac{1}{2\pi} \kappa [\text{curl } \mathbf{v}_s]_z \ln \left( \frac{r_0}{\xi} \right) - 2\Omega v_s r - \frac{\kappa}{\pi} \Omega \right] d^2r. \quad (2)$$

The second term in the integral represents the energy of a vortex line. If different vortex species are present, the circulation  $\kappa_a = \nu_a \kappa_0$ , the inter-vortex distance  $r_a$ , and the core radius  $\xi_a$  become functions of the spatial coordinates (here  $a = 1$  or  $2$ ).

Let us consider a configuration with  $N_1$  SQV lines and  $N_2$  DQV lines. The overall radius  $R_v$  of the vortex cluster is determined by the total circulation:

$$N_1 \kappa_1 + N_2 \kappa_2 = 2\pi \Omega R_v^2. \quad (3)$$

In the stationary state the areal densities of vortex lines are proportional to their circulation,

$$\pi r_1^2 = \frac{\kappa_1}{2\Omega}; \quad \pi r_2^2 = \frac{\kappa_2}{2\Omega}. \quad (4)$$

The average velocity field is  $\mathbf{v}_s = \mathbf{v}_{s0}$  where

$$\mathbf{v}_{s0} = \begin{cases} \mathbf{v}_{rot}, & \text{if } r < R_v \\ \Omega[\hat{\mathbf{z}} \times \mathbf{r}] R_v^2/r^2, & \text{if } r > R_v. \end{cases} \quad (5)$$

The free energy in Eq. (2) is now given by

$$\frac{\tilde{E}}{E_0} = \left( \frac{R_v}{R} \right)^4 \left[ \frac{3}{4} - \ln \left( \frac{R_v}{R} \right) - \left( \frac{R}{R_v} \right)^2 \right] + \frac{S_1 \epsilon_1 + S_2 \epsilon_2}{S} \quad (6)$$

where  $E_0 = \pi \rho_s \Omega^2 R^4$ ,  $S = \pi R^2$ , and  $S_a = \kappa_a N_a / (2\Omega)$  is the area occupied by SQV or DQV lines, such that  $S_1 + S_2 = \pi R_v^2$ . The normalized vortex-line energy densities in the logarithmic approximation (see Eq. (19)) are

$$\epsilon_1 = \frac{r_1^2}{R^2} \ln \left( \frac{r_1}{\sqrt{e} \xi_1} \right); \quad \epsilon_2 = \frac{r_2^2}{R^2} \ln \left( \frac{r_2}{\sqrt{e} \xi_2} \right). \quad (7)$$

These are proportional to the first power of  $\kappa_a$  as distinct from the single-vortex energy which is proportional to  $\kappa_a^2$  (where  $a = 1$  or  $2$ ).

These expressions are valid when  $r_a \gg \xi_a$  [11]. The energy densities of SQV and DQV arrays become equal when

$$\left(\frac{\kappa_1}{2\pi\Omega\epsilon\xi_1^2}\right)^{\kappa_1} = \left(\frac{\kappa_2}{2\pi\Omega\epsilon\xi_2^2}\right)^{\kappa_2}.$$

The rotation velocity for the transition becomes

$$\Omega^* = \frac{2\kappa_0}{\pi e} \frac{\xi_1^2}{\xi_2^4}. \quad (8)$$

To explore the consequences from the continuum approximation further, we minimize the energy in Eq. (6) with respect to variations of both  $N_1$  and  $N_2$ . This gives the equilibrium configuration, which one would expect to find after an adiabatic transition at constant rotation from the normal to the superfluid state. Several conclusions follow:

(1) If  $\epsilon_2 > \epsilon_1$ , only SQV lines remain since  $S_2$  shrinks to zero (Eq. (6)). In the opposite case,  $S_1$  shrinks to zero, and only DQV lines remain. The DQV becomes more favorable, when  $\Omega > \Omega^*$ . According to our measurements this occurs above 0.6 rad/s (Sec. V A 1).

(2) The radius  $R_v$  of the cluster has its equilibrium value when the width of the surrounding vortex-free CF annulus becomes

$$d_{a(eq)} = R\sqrt{\epsilon_a/2}. \quad (9)$$

where the outer boundary of the cluster consists of type  $a$  vortices.

(3) The energy in Eq. (6) does not depend on the configuration of the vortex cluster with given  $N_1$  and  $N_2$ . Consequently, the continuum approximation in the logarithmic limit does not discriminate between different vortex cluster configurations.

## B. Discrete vortex lines

### 1. Sequentially formed arrays

The continuum approximation in Eq. (6) does not include the surface energies at the interfaces between the vortex cluster and the vortex-free region or between segregated domains occupied by different vortex species. Nor does it account for interactions between individual vortex lines and the container wall. To identify configuration-dependent contributions to the free energy, we need to look at vortex clusters composed of discrete vortex lines. We perform numerical calculations on vortex arrays which consist of  $N_j$  discrete rectilinear vortex lines with coordinates  $\mathbf{r}_j$ , circulations  $\kappa_j = \nu_j\kappa_0$ , where

$\nu_j = 1, 2$ , and core radii  $\xi(j)$ . The superfluid velocity produced by the lines is

$$\mathbf{v}_s = \hat{\mathbf{z}} \times \sum_j \frac{\kappa_j}{2\pi} \left[ \frac{(\mathbf{r} - \mathbf{r}_j)}{|\mathbf{r} - \mathbf{r}_j|^2} - \frac{(\mathbf{r} - \mathbf{r}'_j)}{|\mathbf{r} - \mathbf{r}'_j|^2} \right]. \quad (10)$$

The last term accounts for the image vortices with coordinates  $\mathbf{r}'_j = \mathbf{r}_j R^2/r_j^2$ , of which each one corresponds to one true vortex located at  $\mathbf{r}_j$ .

The interaction potential for vortex lines in the rotating superfluid is equivalent to the Coulomb potential between charged lines immersed into a uniform background charge of opposite sign. The density of the background charge is proportional to  $\Omega$ . The potential acting on each line is the sum of the potentials of the background charge, of the direct logarithmic Coulomb interline interaction, and the interactions with the wall reflections.

The equation describing the dynamics of vortex lines has the form

$$\dot{\mathbf{r}}_j = (1 - b') \mathbf{v}'_s - b[\hat{\mathbf{z}} \times \mathbf{v}'_s], \quad (11)$$

where  $\dot{\mathbf{r}}_j$  is the velocity of the  $j$ th vortex line and  $\mathbf{v}'_s$  the superfluid velocity produced by all other vortices at the position of the  $j$ th reference line, while  $b$  and  $b'$  are the reduced Hall–Vinen mutual friction parameters [13].

To illustrate the dynamic simulation in vortex array formation, we consider a standard experiment when a vortex array is formed in the superfluid state by increasing slowly the rotation velocity linearly from zero [1]. In this process one vortex line is formed after another periodically, every time when the CF velocity at the cylindrical wall exceeds a constant critical value. Fig. 1 illustrates a typical final configuration for such a cluster which includes only one species of vortex lines. They are introduced at a fixed nucleation center, once the CF velocity reaches the critical value.

To simplify matters we may here think of the nucleation center in the form of a line source parallel to the rotation axis, located close to the cylindrical wall of the container [1]. From the nucleation center the newly created rectilinear vortex line moves to the edge of the vortex cluster under the action of the background potential of uniform rotation along a spiral trajectory, which depends on the values of the mutual friction parameters  $b$  and  $b'$ . The line is incorporated into the cluster by pushing via the repulsive interactions, which leads to plastic deformations in the existing array. The final structure of the array resembles in the central region a hexagonal lattice with a large number of dislocations. The lines in the periphery form circular rings which are separated by a wide transition region from the central crystal.

A second variation of the same calculation, but now for a two-component vortex array, is shown in Fig. 2. Again the final state is shown, after DQV lines have been accumulated one by one into an existing cluster of SQV

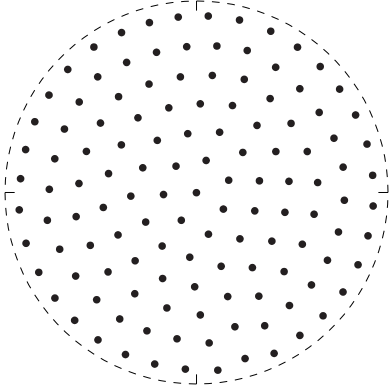


FIG. 1. Computer simulation of vortex array formation. Here  $N_1 = 127$  rectilinear SQV lines have been accumulated one by one to form a cluster, by increasing  $\Omega$  slowly in the superfluid state. The equation of motion (11) with  $b' = 0$  has been used. The nucleation center, from where the lines are injected, is located at the cylinder wall at  $x = R$  (not shown) and  $y = 0$ . The final configuration of the array in the cylindrical container is shown. The dashed circle marks the edge of the cluster at  $r = R_v$ . In the center the lines form a 2D hexagonal crystal with a large number of dislocations, whereas towards the perimeter the configuration deforms to circular concentric rings.

lines. Despite large plastic deformations in the cluster, the injected DQV vortex lines form a compact drop. We observe neither a periodic (chemical) or irregular structure of single DQV lines inside the SQV array. Instead this simulation procedure gives a glassy vortex agglomerate with hexagonal coordination, which is consistent with the experimental situation in  $^3\text{He-A}$  (as will be seen below by comparing eg. with Fig. 14).

To explain these results let us first consider the energy of mixing in different periodic vortex structures, with two types of vortices in the unit cell. Fig. 3 shows the difference between the free energy (per vortex line) of some periodic structures (with up to 9 vortices per unit cell) and the sum of the energies of two separate perfect hexagonal crystals formed from SQV and DQV lines. The values in Fig. 3 have been obtained using the planar summation method from Ref. [14]. We see that for all these structures the energy of mixing is positive – the lowest energy corresponds to two simple hexagonal separated lattices. This fact explains the tendency to form a compact pocket of DQV lines inserted into the SQV array.

The second feature of the simulation is that the equation of motion (Eq. (11)) does not include any thermal annealing process. This, in fact, corresponds to the situation in superfluid  $^3\text{He}$ : Thermal fluctuations are weak, because of the very low temperatures compared to high energy barriers, associated with variations in the superfluid velocity field. The above arrays are therefore not

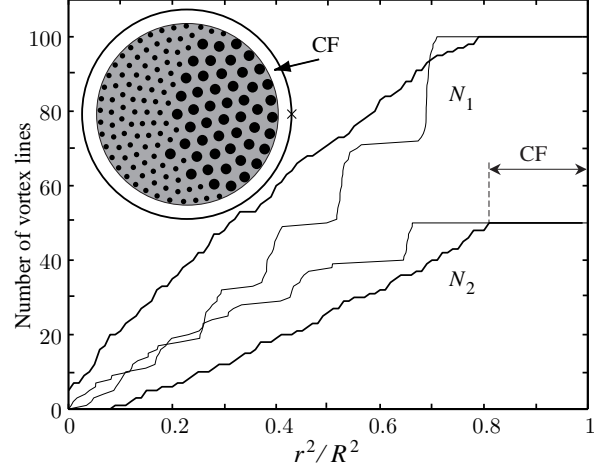


FIG. 2. Simulation calculation of an array with 100 SQV and 50 DQV lines. The DQV lines have been accumulated one by one to an existing equilibrium array of SQV lines, similar to the experiment in Fig. 14. The nucleation center, from where the DQV lines are injected, is located on the cylindrical wall ( $x = R, y = 0$ ) and is marked with a cross in the *inset* where the final configuration of the array at 0.49 rad/s is shown. With this number of vortices the array would correspond to equilibrium circulation at 0.34 rad/s. The thin curves in the *main panel* represent the radial locations of the SQV and DQV lines in the array:  $N_a(r) = \sum_j (x_{a,j}^2 + y_{a,j}^2)$ . They illustrate how the locations of the vortex lines concentrate with increasing radius more and more on concentric rings, although the nearest-neighbor coordination is still triangular, as seen in the *inset*. The thick curves correspond to deceleration records ( $\Omega : 0.49 \text{ rad/s} \rightarrow 0$ ), similar to those measured in the experiment (Fig. 14), and give the average radial distributions  $N_1(r^2)$  and  $N_2(r^2)$ .

expected to have the optimal structure of the global free energy minimum.

## 2. Equilibrium arrays

Experimentally the above simulations correspond to a situation where the container with superfluid  $^3\text{He-A}$  is slowly accelerated to rotation at constant temperature below  $T_c$ . Cooling the container through  $T_c$  in rotation at constant  $\Omega$  is expected to produce a different situation, the global free-energy minimum. To find this state, we now compare the free energies of different vortex array configurations. First we note that for evaluating integrals such as those in Eq. (10) it is useful to introduce a vortex-core cutoff at short distances such that close to the core of the  $j$ th vortex we replace

$$\frac{\mathbf{r} - \mathbf{r}_j}{|\mathbf{r} - \mathbf{r}_j|^2} \rightarrow \frac{\mathbf{r} - \mathbf{r}_j}{\xi_j^2}, \quad (12)$$

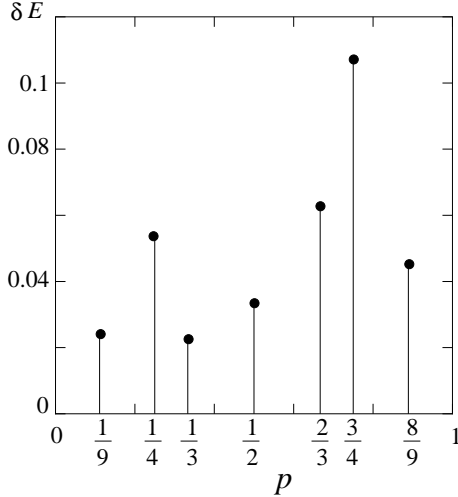


FIG. 3. Energy of mixing  $\delta E$  of different periodic 2D vortex line lattices, formed from SQV and DQV lines. The zero level corresponds to the energy of two separated hexagonal SQV and DQV lattices. The unit cell includes  $N_1$  SQV and  $N_2$  DQV lines. The horizontal axis gives the fraction  $p = N_2/N_c$ , where  $N_c = N_1 + N_2$ . The energy of mixing  $\delta E$  is expressed in units of  $\rho_s \kappa_0^2 / (2\pi N_c)$ . The lattices with  $N_c = 2$  and  $N_c = 4$  have a square unit cell, while all other lattices are obtained by inserting the additional vortex lines into a hexagonal cell.

where  $|\mathbf{r} - \mathbf{r}_j| < \xi_j$ . Using Eq. (10) and performing integration by part, while neglecting all terms of order  $(\xi_a/r_a)^2$  since  $\xi_a \ll r_a$  is assumed, we can rewrite Eq. (1) in the form

$$\begin{aligned} \tilde{E}(\mathbf{v}_s) = & \sum_j \left[ \frac{\rho_s \kappa_j^2}{4\pi} \left( \ln \left| \frac{r_j^2 - R^2}{R \xi_j} \right| + \frac{1}{4} \right) \right. \\ & \left. + \sum_{j \neq l} \frac{\rho_s \kappa_j \kappa_l}{4\pi} \ln \left( \frac{|\mathbf{r}_l - \mathbf{r}'_j| r_j}{|\mathbf{r}_l - \mathbf{r}_j| R} \right) \right] \\ & + \sum_j \frac{\rho_s \Omega \kappa_j}{2} (r_j^2 - R^2). \end{aligned} \quad (13)$$

Next it becomes useful to introduce a vortex lattice energy which provides a more sensitive measure of the configuration dependent energy differences. Let us construct the same free energy as in Eq. (1) but with the superfluid velocity written in the continuum approximation with  $\mathbf{v}_s = \mathbf{v}_{s0}$ , where  $\mathbf{v}_{s0}$  is defined in Eq. (5). The free energy in the continuum approximation is then (cf. Eq. (6))

$$\begin{aligned} \tilde{E}\{\mathbf{v}_{s0}\} &= \frac{\rho_s}{2} \int_0^R (\mathbf{v}_{s0}^2 - 2\mathbf{v}_{s0} \mathbf{v}_{\text{rot}}) d^2 r \\ &= E_0 \left( \frac{R_v}{R} \right)^4 \left[ \frac{3}{4} - \ln \left( \frac{R_v}{R} \right) - \left( \frac{R_v}{R} \right)^{-2} \right]. \end{aligned} \quad (14)$$

The difference of the two energies is the Madelung energy,

$$E_M = \tilde{E}\{\mathbf{v}_s\} - \tilde{E}\{\mathbf{v}_{s0}\}. \quad (15)$$

The Madelung energy represents the vortex lattice contribution and includes the interactions with the image vortices. If one neglects the difference  $\mathbf{v}_s - \mathbf{v}_{s0}$  in the vortex-free region,

$$E_M = \frac{\rho_s}{2} \int_0^{R_v} (\mathbf{v}_s - \mathbf{v}_{s0})^2 d^2 r. \quad (16)$$

Within the logarithmic approximation it reduces to the last term in Eq. (6).

An important feature is the interaction with walls. By moving the wall further from the vortex cluster its influence is reduced and the vortex cluster starts to approach “ideal matter” with more universal properties, similar to point charges in an ion trap. Consider the outermost ring of vortex lines in an ideal coaxial cluster. Nonuniformities in the velocity field around the cluster, which arise from the discrete nature of the vortex lines in the outer ring, decay as  $\sim \exp(-2\pi\delta r/r_a)$  with distance  $\delta r$  from the outer boundary [15]. Conversely, the interaction of the outermost vortex ring with its reflection is of order  $\exp(-4\pi d/r_a)$ , where  $d$  is the distance between the ring and the container wall. To reduce this effect, we take the container radius  $R$  to be clearly larger than  $R_v$  in our simulation calculations. We then obtain an estimate for the Madelung energy which does not depend on the interaction of the particular vortex array with the container wall.

Let us consider an array consisting of only one type of vortex lines (e.g.  $a$ ). We expect that ideally the minimum energy at large  $N_a$  is reached with a configuration with hexagonal structure in the center of the cluster, circular rings at the outer boundary, and an intermediate irregular region between these two regimes. In Eq. (16)  $\mathbf{v}_{s0}$  is the average superfluid velocity within the cluster, equal to the velocity of rotation (Eq. (5)), and thus  $\mathbf{v}_s - \mathbf{v}_{s0}$  represents the deviation from the average in the rotating coordinate system. In an ideal periodic structure this velocity is also a periodic function of the coordinates and the integration in Eq. (16) is reduced to one over a single unit cell:

$$E_M/N_a = \frac{\rho_s}{2} \int_{\text{cell}} (\mathbf{v}_s - \mathbf{v}_{s0})^2 d^2 r. \quad (17)$$

As a first approximation we may replace the hexagonal lattice cell with a cylindrical Wigner-Seitz cell of the same area. The area per vortex is  $b_a^2 \sqrt{3}/2 = \pi r_a^2$ , which gives  $b_a = 1.9046 r_a$  as the relation between the lattice constants  $b_a$  of a 2D hexagonal lattice and  $r_a$  of a cylindrical WS lattice. We refer to this approximation as the WS cylinder. The periodicity of the lattice requires that the component of  $\mathbf{v}_s - \mathbf{v}_{s0}$ , which is normal to the border

of the unit cell, vanishes at the border. In the rotating coordinate frame the superfluid velocity has only an azimuthal component and we may write

$$|\mathbf{v}_s - \mathbf{v}_{s0}| = \begin{cases} \kappa_a r / (2\pi \xi_a^2), & \text{if } r < \xi_a \\ \kappa_a / (2\pi r) - \Omega r, & \text{if } \xi_a < r < r_a. \end{cases} \quad (18)$$

The Madelung energy can then be written as the energy of a single vortex

$$E_M/N_a = \frac{\rho_s \kappa_a^2}{4\pi} \left[ \ln \frac{r_a}{\xi_a} - \alpha_M \right], \quad (19)$$

where  $\alpha_M$  will be referred to as the Madelung constant. For the WS-cylinder approximation in Eq. (18),  $\alpha_M = 1/2$ . Comparing Eqs. (6) and (19) we obtain the expression for the energy density  $\epsilon_a$  through the Madelung energy as in Eq. (7). The Madelung constant  $\alpha_M$  and the Madelung energy can be calculated exactly using the method of planar summation as in Ref. [14]. For an ideal hexagonal structure it yields  $\alpha_M = 0.49877$ . This value is very close to that of the WS-cylinder approximation:  $\alpha_M = 1/2$ .

The Madelung energy in Eq. (15) for large, but finite  $N_a$  can be expanded in powers of the small variable  $b_a/R_v$ :

$$E_M = \frac{\rho_s \kappa_a^2}{2\pi} \left[ \frac{1}{2} \left( \ln \frac{r_a}{\xi_a} - \alpha_M \right) N_a + 2\pi \beta R_v / b_a \right]. \quad (20)$$

Here the first term within the square brackets is the volume contribution, and the term proportional to  $\beta$  is the surface energy per unit vortex length

$$\sigma_a = \frac{\rho_s \kappa_a^2 \beta}{2\pi b_a}. \quad (21)$$

The number of vortex lines in the outermost ring is  $2\pi R_v / b_a$ , where the intervortex distance  $b_a$  is roughly equal to the lattice constant of the ideal hexagonal structure:  $b_a \approx 1.90 r_a$ . One can check that the factor  $\beta$  is independent of the type of vortex as long as the interaction of the vortex lines with the cylinder wall can be neglected.

To determine the surface energy factor  $\beta$ , we calculate  $E_M$  numerically for different values of  $N_a$ . This requires minimization of the free energy in Eq. (13) for different values of  $N_a$ . Here we use the simulated annealing method from Ref. [15] where it was applied to calculate the energy of a large 3D ion cluster in an ion trap. First the vortex lines with a fictitious mass are heated to some ‘‘temperature’’ which is modeled by a random force. The cooling is modeled by inserting a small viscous term in a ‘‘Newtonian equation of motion’’. The heating–cooling cycles are repeated, to allow the array to converge, as a function of time, towards some minimum-energy configuration with a fixed number of vortex lines. Eq. (13) is then used to calculate the free energy of the final

converged optimum configuration. Its Madelung energy is obtained from Eq. (15). Note that plastic deformations play an important role in making relaxation possible towards the energy minimum. The (logarithmic) 2D Coulomb interaction can be regarded as a soft-core potential, in contrast to a hard–sphere interaction of eg. the Lennard-Jones type. This simplifies the relaxation of the vortex array towards an optimal structure. Moreover, in contrast to 3D Coulomb systems, where many crystal structures (bcc, fcc, hcp) have nearly the same energy, the energy of a 2D hexagonal crystal is lower than the energy of most other structures.

Fig. 4 shows the Madelung energy  $E_M/N_1$  per vortex as a function of  $r_1/R_v = 1/\sqrt{N_1}$ , for arrays consisting of SQV lines. We start the simulation from an ideal hexagonal lattice within a circle  $r < R_v$  and after many ( $\sim 10^2$ ) heating–cooling cycles we arrive at the structure which corresponds to a stable minimum of Eq. (13). By repeating this procedure for different values of  $R_v$  (or  $N_1$ ), we obtain  $\beta$  in Eq. (20) from the fitted slope in Fig. 4:  $\beta = 0.010$ . The calculated optimal structure of these vortex clusters (Fig. 5) approaches that of an ideal hexagonal lattice in the center, but then distorts to a quasi-circular structure towards the outer boundary, with a transition region between these two extremes.

Similar simulations for the equilibrium state of a cluster with two coexisting vortex species are more delicate. First, we have already noted that the energy of a mixture of SQV and DQV lines is higher than that of two segregated domains. Secondly, it follows from Eq. (21) that the surface energy of a DQV cluster is  $2\sqrt{2}$  times larger than that of a SQV cluster with the same value of  $R_v$ , i.e.,  $\sigma_2/\sigma_1 = 2\sqrt{2}$  because  $\kappa_2 = 2\kappa_1$  and  $r_2 = \sqrt{2}r_1$ . Hence, the only configurations, which were found to converge towards a stable minimum-energy state, are coaxial clusters with the DQV lines in the center, surrounded by an outer annulus of SQV lines. In Fig. 6 the Madelung energy  $E_M/N$  per circulation quantum of such clusters has been plotted vs.  $r_1/R_v = 1/\sqrt{N}$ , where  $N = N_1 + 2N_2$  is the total number of circulation quanta. We take here  $N_1 = 2N_2$  and thus the interface separating the two types of vortex lines lies at  $r \approx R_v/\sqrt{2}$ . The optimal structure (Fig. 7) turns out to consist of a nearly ideal hexagonal lattice of DQV lines, which extends all the way from the center to the inner interface. At the inner interface the mismatch in periodicity between the two vortex species,  $b_2 = \sqrt{2}b_1$ , creates an abrupt break, but the smaller SQV lines very effectively compensate for the faults on the boundary of the central hexagonal DQV crystal. Also the SQV lines fulfill the boundary condition and on approaching the outer boundary of the cluster a perfect circular ring structure is established.

Simulation attempts on the inverse initial state, namely on segregated coaxial domains but with the SQV lines in the center, were not successful. Such calculations are slow in convergence since they start to drift towards

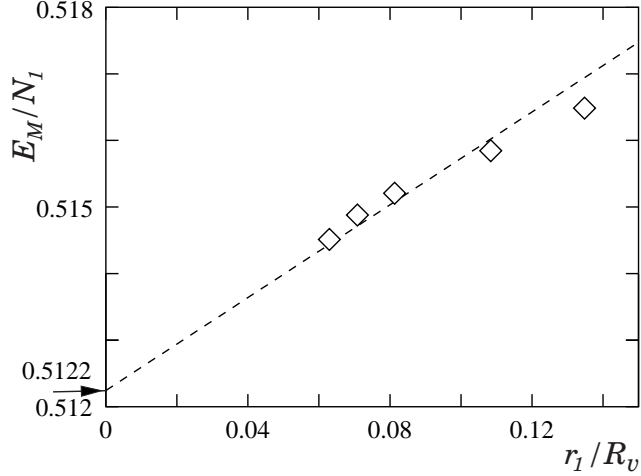


FIG. 4. Madelung energy  $E_M$  for an equilibrium cluster of SQV lines, plotted as a function of  $r_1/R_v = 1/\sqrt{N_1}$  (where  $N_1 = 55, 85, 151, 199, \text{ and } 253$ ). The calculations represent the minimum value of  $E_M/N_1$  (in units of  $\rho_s \kappa_0^2/2\pi$ ) after a large number of simulated annealing cycles. The container radius is set at  $R = 40r_1$  while the core radius is fixed to  $\xi_1/r_1 = 0.218$ . The latter corresponds to SQV lines with  $\xi_1 = 32\mu\text{m}$  at  $\Omega = 0.5 \text{ rad/s}$ . The dashed line represents the linear dependence of Eq. (20) and the fitted slope gives for  $\beta$  the value :  $\beta = 0.010$ . The extrapolation  $E_M/N_1 = 0.512$  to an infinite vortex array equals that which one obtains from Eq. (19) for an ideal hexagonal lattice.

the ideal structure where the SQV lines are in the outer periphery. The same applies to asymmetric starting configurations, such as the one where the cluster is divided along its diameter into equal halves with only SQV and DQV lines in each. This arrangement does not minimize the outer surface energy or allow for the presence of a symmetric hexagonal crystal in the center of the array.

We can use the results in Fig. 6 to estimate the surface energy of the inner interface  $\sigma_{12}$ . The dashed line shows a fit to the calculations:  $E_M(DQV + SQV)/N = 0.7294 + 0.0462 r_1/R_v$  (in units of  $\rho_s \kappa^2/2\pi$ ). The same fit to the SQV clusters in Fig. 4 gives  $E_M(SQV)/N = 0.5122 + 0.0348 r_1/R_v$ . Since the outer shell in both cases consists of SQV lines only, we can associate the difference in slopes with the surface energy of the inner interface between the SQV and DQV domains. This gives  $\delta E_{12}/N = 0.012 r_1/R_v$ . Taking into account the length  $2\pi R_2 \approx 2\pi R_v/\sqrt{2}$  of the interface, we obtain  $\sigma_{12}/\sigma_1 \approx 0.48$ . Remembering that  $\sigma_2/\sigma_1 = 2.83$ , we find that  $\sigma_2 > \sigma_1 + \sigma_{1,2}$ . Thus the contact angle between the SQV domain and the vortex-free CF annulus has to be zero: the SQV domain “wets” completely the vortex-free region. The most preferable configuration is therefore one where the DQV domain is completely surrounded by

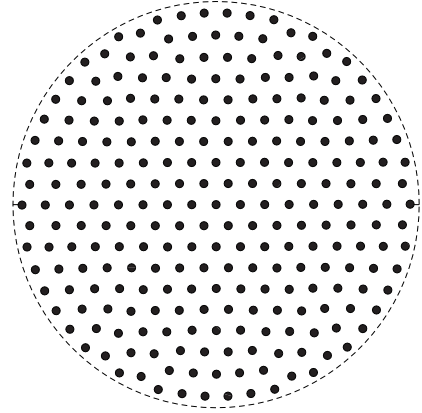


FIG. 5. Calculated minimum-energy structure of a SQV cluster with  $N_1 = 253$  lines. This is one of the examples in Fig. 4. The dashed circle marks the edge of the cluster at  $r = R_v$ . The container wall is further out at  $R = 2.5R_v$ . This is thus a metastable state with less than the equilibrium number of vortex lines, but with the cluster itself at equilibrium density. All calculated clusters in Fig. 4 are of this type, to reduce the influence of the cylinder wall on the simulation calculations.

SQV lines.

Interestingly the reduced surface energy with SQV lines makes the coexistence of DQV and SQV lines possible even in a region of the SQV – DQV phase diagram where the global energy minimum corresponds to that of DQV lines only. The energy of a cluster consisting of DQV lines only is given by Eq. (20),

$$E_M^{(2)} = \frac{\rho_s \kappa_2^2 R_v^2}{4\pi r_2^2} \left( \ln \frac{r_2}{\xi_2} - \alpha_M \right) + 2\pi R_v \sigma_2 ,$$

while the energy of a cluster with a central DQV domain surrounded by SQV lines is

$$E_M^{(21)} = \frac{\rho_s \kappa_2^2 R_2^2}{4\pi r_2^2} \left( \ln \frac{r_2}{\xi_2} - \alpha_M \right) + \frac{\rho_s \kappa_1^2 (R_v^2 - R_2^2)}{4\pi r_1^2} \left( \ln \frac{r_1}{\xi_1} - \alpha_M \right) + 2\pi R_v \sigma_1 + 2\pi R_2 \sigma_{12} .$$

$E_M^{(21)}$  as a function of  $R_2$  has a minimum at  $R_2 = 0$  for  $\Omega < \Omega^*$ , when a SQV cluster is more favorable. However, due to a finite  $\sigma_{12}$ , there is still a minimum at  $R_2 = 0$  even when  $\Omega > \Omega^*$ , i.e. when a DQV cluster is more favorable. In this second case another minimum appears at  $R_2 = R_v$  which corresponds to a DQV cluster surrounded by a thin surface layer of SQV lines. Indeed, the energy  $E_M^{(21)}$  is a decreasing function of  $R_2$  in the region  $R_2 \sim R_v$ . For  $R_2 = R_v$  it is smaller than  $E_M^{(2)}$  because  $\sigma_2 > \sigma_1 + \sigma_{12}$ . The difference  $\delta E = E_M^{(21)} - E_M^{(2)}$  for  $\Omega > \Omega^*$  is shown in

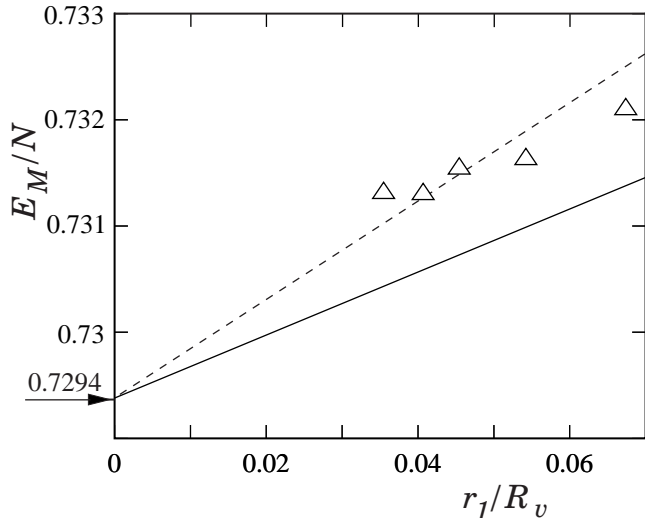


FIG. 6. Calculated Madelung energy per circulation quantum,  $E_M/N$ , for segregated coaxial minimum-energy clusters, composed of SQV and DQV lines, plotted as a function of the inverse of the normalized cluster radius:  $r_1/R_v = 1/\sqrt{N}$ . In the minimum energy configuration the DQV lines are in the center. Here the total circulation of the DQV lines has been taken to be equal to that of the SQV lines (i.e.  $N_1 = 2N_2 = N/2$ ).  $E_M$  is expressed in units of  $\rho_s \kappa_0^2 / 2\pi$  and is calculated for five cluster radii  $N_2 = 55, 85, 121, 151$ , and 199. The parameters are  $\xi_1/r_1 = 0.218$ ,  $\xi_2/r_1 = 0.236$ , which correspond to  $\xi_1 = 32 \mu\text{m}$  and  $\xi_2 = 49 \mu\text{m}$  at  $\Omega = 0.5 \text{ rad/s}$ . The container radius is set to  $R = 40 r_1 = 5.8 \text{ mm}$ . The arrow indicates the sum of the Madelung energies in Eq. (20) for infinite SQV and DQV lattices,  $(E_{M1} + E_{M2})/N$  in the limit  $N \rightarrow \infty$ , when the surface energy can be neglected. The solid line has the same slope as the line in Fig. 4 and represents the surface energy of the outer boundary of a cluster with SQV lines. The dashed line is a linear fit through the data points.

Fig. 8 as a function of  $R_2/R_v$ . The two local minima at  $R_2 = 0$  and  $R_2 \approx R_v$  have the same energy when

$$\Omega^\dagger = \Omega^* \left[ 1 + \frac{8\pi\beta r_1^2 \sigma_{12}}{R_v b_1 \sigma_1} \right]. \quad (22)$$

Here  $\Omega^*$  is determined by Eq. (8) where, however,  $e$  should be replaced with the more accurate expression  $e^{2\alpha_M}$  of an ideal vortex lattice.  $\Omega^\dagger$  is only slightly higher than  $\Omega^*$  because of the large value of  $R_v/r_1$ .

Eq. (22) states the condition for the global equilibrium between SQV and DQV lines. However, because of the minimum at  $R \approx R_v$ , the model allows for the coexistence of the two vortex species: A “monolayer” in the form of an outer circle of SQV lines could surround a DQV cluster, when  $\Omega > \Omega^*$ . Evidently, our idealized model only applies if the vortex layer is at least a few inter-vortex distances wide. With this warning we note that

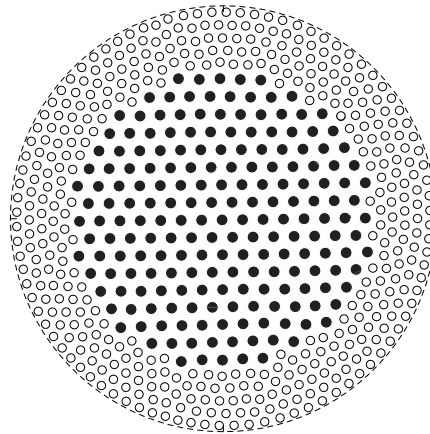


FIG. 7. Calculated minimum-energy structure of a cluster with  $N_2 = 199$  and  $N_1 = 2N_2$  lines. This is one of the examples from Fig. 6. The dashed circle denotes the edge of the cluster at  $r = R_v$  while the container wall is at  $R = 1.4R_v$ .

the qualitative behavior of  $\delta E$  is shown in Fig. 8 by the solid line, when an outer boundary layer of SQV lines is present.

Summarizing our analysis we conclude that the minimum energy configuration for coexisting SQV and DQV lines in a rotating cylinder can only be established by considering discrete vortex arrays. The optimal configuration (1) consists of segregated domains, (2) has cylindrical symmetry (3) with the SQV lines forming the outer boundary of the cluster.

#### IV. EXPERIMENTAL METHOD

The structure of the vortex cluster in the rotating container is probed with cw NMR. It allows one to determine the average radial composition, i.e.  $N_1(r^2)$  and  $N_2(r^2)$ . The NMR method is based on a measurement of the absorption spectrum to which SQV and DQV lines each contribute a characteristic satellite peak. These satellites have frequency shifts which are different from each other and from the bulk liquid NMR line [16]. Both the peak height and the integrated intensity of the satellites are proportional to the total number  $N_a$  of vortex lines of the species ( $a$ ) and can be calibrated to give the absolute value of  $N_a$ .

To measure the composition of a vortex cluster we monitor the peak height of a satellite as a function of the rotation velocity  $\Omega$  during slow deceleration, when the cluster expands and the outermost vortex lines annihilate one by one at the cylinder wall [17]. The peak height as a function of  $\Omega$  gives the number of the annihilating vortex lines as a function of  $r^2$ . We can thus reconstruct



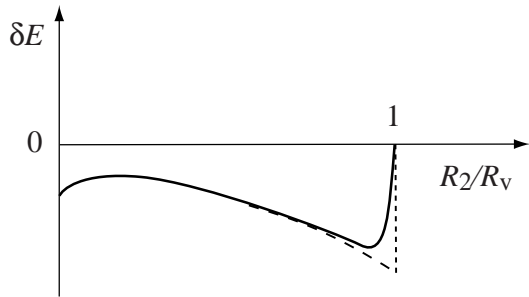


FIG. 8. Free energy difference  $\delta E$  between a DQV cluster with radius  $R_2$  and one which has an outer surface layer of SQV lines in the region  $R_2 < r < R_v$ , when  $\Omega > \Omega^*$ . Within the idealized model of Eq. (20), there exists a step-like energy reduction by  $2\pi R_v(\sigma_2 - \sigma_1 - \sigma_{12})$  (dotted line), when a thin layer of SQV lines is placed on the outer surface of a DQV cluster. Decreasing the radius  $R_2$  of the DQV domain further results in an increase in the free energy (dashed curve) until it reaches a maximum followed by another minimum at  $R_2 = 0$ . The solid curve indicates schematically the dependence with a SQV surface layer of finite width.

the cumulative number of both types of vortices  $N_a(r^2)$ , which gives the number of vortex lines of type (a) inside a radius  $r$ . Indeed, for reconstructing the radial distributions only one of the peak height dependences  $N_a(r^2)$  needs to be measured. The requirement of solid-body rotation of the superfluid component within the vortex cluster gives the relation:  $N_1(r) + 2N_2(r) = 2\pi r^2 \Omega / \kappa_0$ .

The measurements have been performed with two cylindrical containers, one fabricated from epoxy and the other from fused quartz [18]. Both are right circular cylinders 7 mm long and  $R = 2.5$  mm in radius. They are closed off, except for an orifice of 0.5 mm in diameter, located in the center of the flat bottom plate. The orifice connects to a long tubular channel which provides via its liquid  $^3\text{He}$  column the thermal contact to the refrigerator. The  $^3\text{He}$ -A temperature in the container is determined from the calibrated temperature dependent frequency shift of the bulk liquid NMR absorption peak.

Two controlled ways exist for preparing a vortex cluster: 1) The sequential addition of vortex lines one by one to the cluster by accelerating  $\Omega$  slowly (in the presence of a constant critical velocity), and 2) by cooling in rotation through  $T_c$ . One might expect in the latter case that a sufficiently slow cool down through  $T_c$ , one which approaches the adiabatic limit, will lead to an equilibrium state, where the number and type of vortex lines as well as the configuration of the cluster adjust such that the total energy becomes minimized. This has been experimentally checked with respect to the type of lines [2] and the number of lines [17].

In  $^3\text{He}$ -A the transition between the SQV and DQV lines occurs in the presence of an applied magnetic field

[11] as a function of  $\Omega$  [2]. Experimentally we find that there exists a region of coexistence around this transition, ie. the transition has a width as a function of  $\Omega$  within which both species of vortex lines are present simultaneously, but where their relative amounts depend on  $\Omega$ . Ideally the transition should be sharp and therefore our experimental situation cannot represent the homogeneous adiabatic limit. Nevertheless, in the coexistence regime the energy difference between the two vortex species is small, and, in principle, it can be smaller than the energies associated with the vortex cluster configuration. Therefore, in addition to trying to identify what type of inhomogeneity controls the width of the transition, we may investigate the vortex-array configurations in the coexistence regime and ask whether these energy contributions are minimized in the transition.

The sequentially formed coexistence clusters are more obvious. Only one type of cluster is possible: Due to their much higher critical velocity SQV lines can only be formed by cooling through  $T_c$  in rotation. Thus by cooling slowly through  $T_c$  at low  $\Omega$  an equilibrium cluster of SQV lines is formed, to which DQV lines can be added sequentially by increasing  $\Omega$  slowly at constant temperature below  $T_c$ .

The first observation from our measurements was that the radial distributions of the two vortex species turned out to be different in the equilibrium clusters and the sequentially constructed states. This means that in superfluid  $^3\text{He}$  a common cluster configuration is not realized, but metastable states are long lived and the structure of a vortex cluster depends on how it has been prepared.

## V. MEASUREMENTS

### A. Coexistence regimes of SQV and DQV

#### 1. Dependence on rotation while cooling through $T_c$

When the rotating sample is cooled in the NMR field through  $T_c$ , an equilibrium vortex state with only SQV lines is formed at low rotation,  $\Omega \leq 0.6$  [2]. Above this velocity also DQV lines are created. Their relative number increases with  $\Omega$  until above 3 rad/s no more SQV lines are observed. The number of DQV lines is shown in the coexistence regime as a function of  $\Omega$  in Fig. 9, where each data point ( $\circ$ ) represents  $I_v/I_{tot}$ , the integrated NMR absorption  $I_v$  of the DQV satellite normalized to the total absorption  $I_{tot}$  in the NMR spectrum.

The normalized absorption  $I_v(\Omega)/I_{tot}$  can be translated to vortex line numbers  $N_2(\Omega)$  by comparing to an equilibrium state with only DQV lines. The equilibrium number of vortex lines (of type  $a$  only) is given by

$$N_{a(eq)}(\Omega) = \pi(R - d_{a(eq)})^2 \frac{2\Omega}{\kappa_a} \propto \frac{I_v(\Omega)}{I_{tot}}, \quad (23)$$

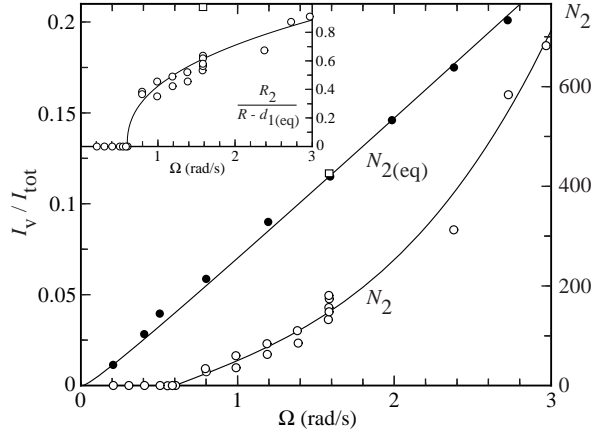


FIG. 9. Coexistence of SQV and DQV lines in the high-field (dipole-unlocked [11]) regime as a function of rotation velocity  $\Omega$ . ( $\circ$ ): Normalized DQV satellite intensity  $I_v/I_{tot}$  plotted as a function of the rotation velocity at which the sample was cooled through  $T_c$ . On the right vertical axis the intensity has been expressed in terms of line numbers,  $N_2(\Omega)$ , by means of the calibration,  $N_{2(eq)}$ . At low  $\Omega$  only SQV lines are formed and  $N_2(\Omega < 0.6 \text{ rad/s}) = 0$ . Above 0.6 rad/s the coexistence regime starts, where the fraction of the total circulation in DQV lines increases with  $\Omega$ , until well above 3 rad/s no more SQV lines are formed. As a guide for the eye, the solid curve represents  $I_v/I_{tot} = 0.033(\Omega - 0.6) + 0.0084(\Omega - 0.6)^3$ . The cool-down rate at  $T_c$  has been kept at  $|dT/dt|_{T_c} \lesssim 5 \mu\text{K/min}$ , except for the data point marked with an open square ( $\square$ ), for which the cooling rate was  $(dT/dt)_{T_c} = -18 \mu\text{K/min}$ . ( $\bullet$ ): Calibration measurement of  $I_v/I_{tot}$  with the equilibrium number of DQV lines,  $N_{2(eq)}$ . The fitted result gives  $I_v(\Omega)/I_{tot} = 2.74 \cdot 10^{-4} N_{2(eq)}(\Omega) \approx 0.0806 \Omega (1 - 0.1/\sqrt{\Omega})$  ( $\Omega$  in rad/s). The *inset* shows the radius of the central DQV cluster in relative units in the coexistence regime, together with a guide for the eye:  $R_2/(R - d_{1(eq)}) = 0.618 (\Omega - 0.6)^{0.41}$ . Other conditions:  $P = 29.3 \text{ bar}$ ,  $H = 9.91 \text{ mT}$ , the satellite intensities have been measured at  $T = 0.81 T_c$ .

where the width  $d_{a(eq)}$  of the equilibrium CF annulus is defined in Eq. (9). The calibration measurement,  $N_{2(eq)}(\Omega)$ , is plotted ( $\bullet$ ) in Fig. 9. In practice, the equilibrium number of vortex lines is equal to that at the annihilation threshold [17]. In Fig. 9 the data for  $N_{2(eq)}(\Omega)$  were measured by first slowly increasing  $\Omega$  from zero to some high velocity  $\Omega > 3.5 \text{ rad/s}$  at  $T = 0.81 T_c$  and by then decelerating sequentially to lower  $\Omega$  values and recording there at constant  $\Omega$  the respective value of  $I_v(\Omega)/I_{tot}$ . The difference between the two curves in Fig. 9 gives the number of SQV lines in the metastable coexistence regime:  $N_1(\Omega) = 2 [N_{2(eq)}(\Omega) - N_2(\Omega)]$ .

The critical rotation velocity  $\Omega^*$  for the transition from SQV to DQV lines lies thus according to Fig. 9 within the interval 0.6 – 3 rad/s. An estimate for  $\Omega^*$  can be worked out from Eq. (8) using the normalized satellite

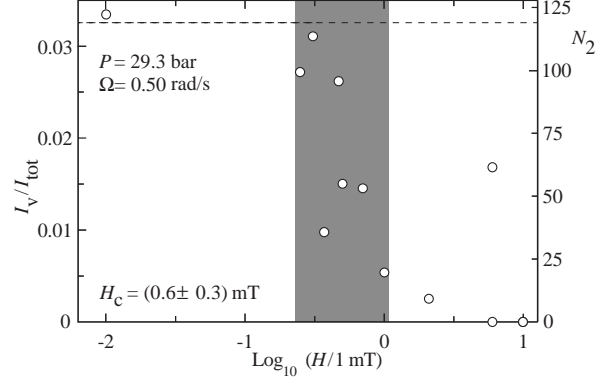


FIG. 10. Coexistence of SQV and DQV lines as a function of magnetic field  $H$  below 0.6 rad/s: Normalized DQV satellite intensity  $I_v/I_{tot}$  plotted vs the field  $H$ , which was applied during cooling through  $T_c$  at 0.5 rad/s. On the right vertical axis the NMR absorption intensity has been converted to DQV vortex numbers,  $N_2(H)$ , using the calibration in Fig. 9. The horizontal dashed line represents the equilibrium number  $N_{2(eq)}$  of DQV lines. The shaded region marks the width of the coexistence regime around the critical field,  $H_c \approx 0.6 \text{ mT}$ . In this measurement the field was increased to the NMR value 9.91 mT in the superfluid state below  $T_c$ , while the sample was cooling to 0.81  $T_c$ , where the intensity  $I_v/I_{tot}$  was measured. Other conditions were the same as in Fig. 9. In the transition through  $T_c$  the equilibrium value of total circulation is created and thus at high field  $H > H_c$ , where  $N_2 \rightarrow 0$  in accordance with the results in Fig. 9, the deficit from  $N_{2(eq)}$  represents the SQV lines.

intensity  $I_v/I_{tot}$ . It measures the effective vortex-core area compared to that of the WS cell [11], or

$$\frac{I_v}{I_{tot}} \approx \left( \frac{\xi_a}{r_a} \right)^2 = \frac{2\pi\xi_a^2}{\kappa_a} \Omega. \quad (24)$$

For the sake of comparison we neglect the temperature dependence of the core radii [11] and use the best values for the satellite intensities, which come from measurements at 0.50  $T_c$  (11.7 mT, and 33.9 bar): In the equilibrium state the coefficient in front of  $\Omega$  in Eq. (24) was found to be 0.094 for SQV and 0.114 for DQV lines. These values give for the soft core radii  $\xi_1 \approx 32 \mu\text{m}$  and  $\xi_2 \approx 49 \mu\text{m}$ . From Eq. (8) we now get  $\Omega^* \approx 2.8 \text{ rad/s}$ , in qualitative agreement with the experiment. The estimate for  $\Omega^*$  in Eq. (8) is based on the differences in quantization number, core size, and the crude approximation for vortex energy in Eq. (7). A more sophisticated numerical calculation in Ref. [6] places  $\Omega^*$  in the interval 0.54 – 1.4 rad/s.

## 2. Dependence on magnetic field while cooling through $T_c$

In addition to  $\Omega$ , the second important variable of the vortex phase diagram is the applied magnetic field  $H$  [19]: When it exceeds the equivalent of the spin-orbit coupling, as is the case in our NMR measurements, the SQV and DQV structures display well-separated vortex cores, with  $r_a \gg \xi_a$  [11]. At low fields the spin-orbit interaction dominates and these vortex structures are not stable. Instead here vorticity appears in the form of extended periodic vortex textures with no core or a much expanded core, such that  $r_a \sim \xi_a$ . The dominant low-field vortex texture has a square lattice and a unit cell with four quanta of circulation [2,6]. These vortex textures are separated from the high-field structures by a transition of first order.

The transition between the low and high field regimes as a function of  $H$  is illustrated by the measurements in Fig. 10. Our NMR is performed at a fixed frequency in the high field limit. Therefore the measurements in Fig. 10 have to follow a particular routine. First, the container is cooled through  $T_c$  at 0.5 rad/s, with the field  $H$  adjusted to the value given on the horizontal axis. Next, below  $T_c$  the field is increased to the NMR value of 9.91 mT. During the field sweep the low field vortex texture undergoes a topological transition to the high-field (dipole-unlocked) DQV structure, with well-separated vortex cores. This transition is not revealed in our measurements, if the field sweep is conducted at high temperatures ( $T > 0.8 T_c$ ). However, the SQV has different topology [11] and any vortices of this kind will remain singly quantized during the field sweep. After the field sweep, the container is cooled to lower temperatures, to improve the resolution in the NMR measurement of the vortex satellites, and the DQV satellite intensity is measured.

As shown in Fig. 10, we find a critical field  $H_c \approx 0.6$  mT. Above  $H_c$  the SQV lines dominate, as required when  $\Omega < 0.6$  rad/s. Below  $H_c$  only DQV lines are found, which represent the transformed low-field vortex textures after the field sweep. Centered around  $H_c$  there is a coexistence regime with a width of 0.5 mT, where both types of vortex lines are present. Within the coexistence regime, the relative abundance of SQV lines increases continuously with increasing  $H$ , similar to the situation in Fig. 9 as a function of  $\Omega$ .

The same behavior is verified in Fig. 11 at a higher rotation velocity of 1 rad/s. On comparing Figs. 10 and 11 it is noted that both  $H_c$  and the width of the coexistence regime increase with  $\Omega$  [2]. In the measurements of Fig. 11 both the DQV and SQV satellite intensities were determined separately. On the low field side only DQV lines are found. On the high field side both types of lines are formed, with a 4 times larger share of the circulation carried by the SQV lines. This is the same ratio as was

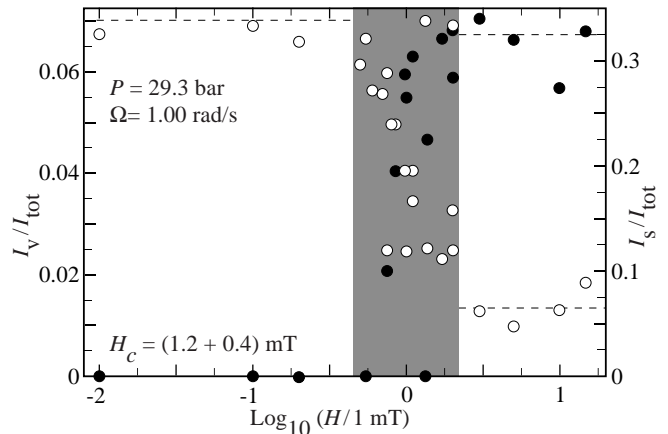


FIG. 11. Coexistence of SQV and DQV lines as a function of magnetic field above 0.6 rad/s: The normalized intensities  $I_v/I_{tot}$  of the DQV satellite ( $\circ$ ; left vertical axis) and  $I_s/I_{tot}$  of the SQV satellite ( $\bullet$ ; right vertical axis) have been plotted as a function of the magnetic field  $H$ , which was applied during cooling through  $T_c$  at 1 rad/s. The horizontal dashed line on the left represents the equilibrium value expected for DQV lines, after a superfluid transition at low fields ( $H < H_c$ ) and a subsequent increase of the field to 9.91 mT. On the right ( $H > H_c$ ), the dashed lines give the mean values for the SQV and DQV lines:  $N_1 \approx 440$  and  $N_2 \approx 48$ . The shaded region marks the width of the transition regime around the critical field,  $H_c \approx 1.2$  mT. The coexistence regime includes both the shaded and the high field regions,  $H > H_c$ . The same conditions apply as in Fig. 9, including the calibration for the DQV satellite intensity. The calibration for the SQV satellite intensity is  $N_{1(eq)}(\Omega) \propto I_s(\Omega)/I_{tot} \approx 0.43 \Omega (1 - 0.089/\sqrt{\Omega})$  ( $\Omega$  in rad/s).

already seen in Fig. 9 at 1 rad/s.

In a magnetic field the superfluid transition splits into  $T_{c1}$  and  $T_{c2}$ . The former is the transition from the normal to the  $A_1$  phase and the latter from  $A_1$  to the  $A_2$  phase, which is the regular  $^3\text{He-A}$ . The thermal width of the  $A_1$  region is narrow, approximately  $0.6 \mu\text{K}$  at 10 mT. We might wonder what effect the intermediate  $A_1$  phase has on the DQV to SQV ratio above  $H_c$  in Figs. 9 – 11: Are more changes to be expected at fields much larger than those shown in Figs. 10 and 11? We find that at least a cool down in 60 mT field at 1.4 rad/s gives the same result as at 10 mT.

## 3. Dependence on cooling rate at $T_c$

Surprisingly in Fig. 9 one data point deviates from the typical behavior (denoted with ( $\square$ ) at 1.6 rad/s). The only distinction that can be appended to its measurement, compared to other data points at the same  $\Omega$ , is a

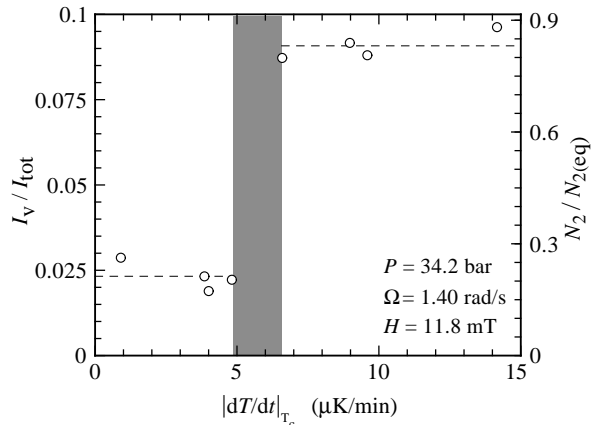


FIG. 12. Influence of cooling rate at  $T_c$  on the relative number of SQV and DQV lines. The left vertical axis gives the normalized DQV satellite intensity  $I_v/I_{tot}$  as a function of cooling rate during the transition through  $T_c$  at 1.4 rad/s. The satellite intensities are measured at  $(0.49 - 0.51) T_c$ , where the calibration for the DQV line satellite is  $N_{2(eq)}(\Omega) \propto I_v(\Omega)/I_{tot} \approx 0.078 \Omega (1 - 0.11/\sqrt{\Omega})$  ( $\Omega$  in rad/s). In this expression  $I_v$  includes only the primary satellite peak (the secondary peak, which is also visible at these low temperatures, is not included in the absorption). On the right vertical axis the calibration has been used to list the fraction of the total circulation in DQV lines,  $N_2/N_{2(eq)}$ , while the rest,  $1 - N_2/N_{2(eq)}$ , is carried by SQV lines.

larger cooling rate during the superfluid transition: The five data points measured at cooling rates  $|dT/dt|_{T_c} = 1 - 5 \mu\text{K}/\text{min}$  give for the relative amount of DQV lines  $N_2/N_{2(eq)} \approx 0.38$  while the anomalous point at a cooling rate of  $18.5 \mu\text{K}/\text{min}$  falls on the equilibrium curve  $N_{2(eq)}$ , with no SQV lines detected at all.

Additional evidence is shown in Fig. 12 on how a faster cooling rate at  $T_c$  shifts vorticity from SQV to DQV lines. In these measurements a fused quartz container was used in which  $^3\text{He-A}$  could be supercooled to below  $0.49 T_c$ . This feature improves the measuring resolution since at lower temperatures the different vortex satellites are separated by larger shifts from each other in the absorption spectrum [16]. When the cooling rate in Fig. 12 at 1.4 rad/s reaches  $5 \mu\text{K}/\text{min}$  a change over takes place from SQV to DQV lines: at lower rates only one fourth of the total circulation is in DQV lines (which is the same fraction as in Fig. 9), while above  $6 \mu\text{K}/\text{min}$ , only few SQV lines are formed. Similar measurements at 0.6 rad/s with cooling rates up to  $16 \mu\text{K}/\text{min}$  did not yet produce a DQV satellite of measurable height.

The quartz container in the measurements of Fig. 12 was thermally connected to the refrigerator via an orifice of 0.5 mm in diameter. Later measurements with another quartz cylinder with a small and long channel of

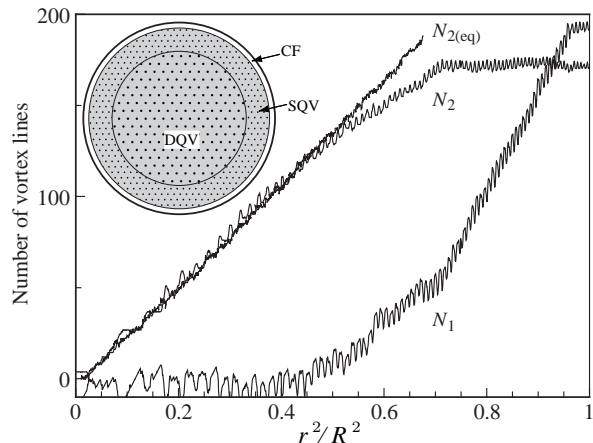


FIG. 13. Radial distributions  $N_1(r^2)$  and  $N_2(r^2)$  after cooling through  $T_c$  at 1 rad/s and 1.1 mT. The deceleration from 1 rad/s to zero is performed at  $0.81 T_c$  and 9.91 mT. Other conditions are the same as in Fig. 14.  $N_{2(eq)}$  shows for comparison the deceleration for an array consisting of only DQV lines. It is prepared by cooling through  $T_c$  at  $\Omega > 1.5$  rad/s in zero field and by then sweeping the field up to 9.91 mT at  $0.81 T_c$ . The final part of the deceleration below 0.7 rad/s is shown here. As demonstrated in Ref. [17], during a slow deceleration ( $d\Omega/dt = -1.5 \cdot 10^{-3} \text{ rad/s}^{-2}$ ) the total circulation at any value of  $\Omega$  corresponds roughly to that in the equilibrium state. The *inset* illustrates schematically a transverse cross section through the rotating container with the coaxial array configuration: the SQV lines (small dots) are in the outer annulus and the DQV lines (large dots) in the center.

0.4 mm diameter displayed appreciably smaller fractions of SQV lines, also in the regime  $\Omega < 0.6$  rad/s where  $N_2 = 0$  in Fig. 9. The narrow and long channel increases the thermal resistance between the sample container and the refrigerator, and leads to rapid irreversible normal-to-superfluid transitions, where the transition velocity cannot reliably be controlled externally. This suggests that a large cooling rate and nonequilibrium conditions enhance the formation of DQV lines at the expense of SQV lines.

There is one data point also in Fig. 10 at 6 mT with a larger fraction of DQV lines than what one would expect on the basis of the general behavior. In the measurements as a function field (Figs. 10 and 11) the cooling rate at  $T_c$  cannot be monitored accurately, since the NMR measurement is inoperative at that stage. Therefore a cooling routine was worked out which should have yielded rates of less than  $5 \mu\text{K}/\text{min}$ . However, without the NMR record it is not possible to state whether a mistake occurred in the cooling routine of the anomalous data point in Fig. 10.

## B. Vortex cluster in coexistence regime

The radial composition of a cluster with both SQV and DQV lines can be determined by recording the amplitudes of the satellites as a function of  $\Omega$  while the rotation is slowly decelerated. In Fig. 13 the result is shown for an array which has been created by cooling through  $T_c$  at 1 rad/s. Here the distributions of the two vortex species are segregated: The SQV lines annihilate first and the DQV lines later. This behavior corresponds to the coaxial array structure, shown in the inset of Fig. 13, which consists of a central region of 130 DQV lines, a peripheral annulus of 140 SQV lines, and the exterior vortex-free CF region of equilibrium width. The boundary between the DQV and SQV regions is relatively sharp (10% of the radius of the array, or additionally roughly 40 DQV and 50 SQV lines).

The coaxial configuration is stable against externally applied perturbations. In fact, no means were found to change the configuration, without removing vortex lines by deceleration or by adding new ones during acceleration. The noise in the rotation drive is of order  $|\Delta\Omega| \sim 1 \cdot 10^{-3}$  rad/s. However, no noticeable changes in the coaxial configuration were observed when the array is maintained for several hours at constant  $\Omega$ . This is not surprising since even a sinusoidal modulation of  $\Omega$  with an amplitude  $\Delta\Omega \sim 0.1$  rad/s does not cause measurable changes. (The modulation by  $2\Delta\Omega$  is less than the separation between the annihilation and critical velocity thresholds and thus the number of vortex lines is not yet changed.) This suggests that any spontaneous re-ordering of the two vortex species within the array from the segregated domain structure to a mixed configuration is below our measuring resolution. Thus the cool down from  $T_c$  to the measuring temperature or a magnetic field sweep after the transition through  $T_c$  are not expected to introduce changes in the array configuration.

The segregation into two coaxial domains, with the SQV lines in the outer annulus, is always observed when both vortex species are found to coexist after cooling through  $T_c$ . We also find, by measuring the width of the CF annulus [17], that the total number of lines adjusts itself so that the energy in Eq. (6) is minimized. This is expected, since the total circulation corresponds to a dominant energy term. In comparison the structure of an individual vortex line or the spatial distribution of the two vortex species within the array, represent much smaller energy contributions.

## C. Sequentially formed vortex cluster

The stability of vortex arrays in superfluid  $^3\text{He}$  can also be approached from the other extreme, by studying the disorder in artificially constructed arrays of coexisting

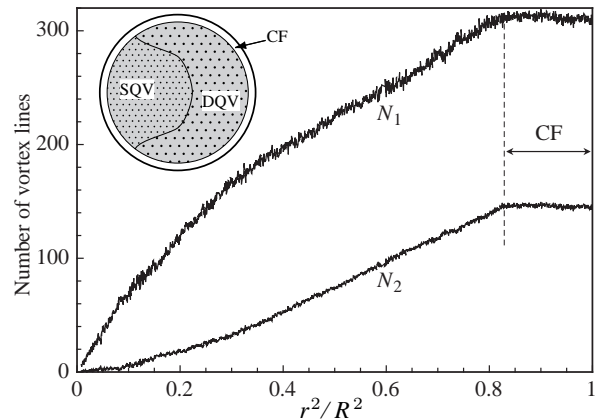


FIG. 14. Radial distributions  $N_1(r^2)$  and  $N_2(r^2)$  in a sequentially formed vortex cluster. The original array was an equilibrium state of SQV lines, to which DQV lines were added later by increasing rotation in the superfluid state. The SQV array was prepared at 29.3 bar pressure and 9.91 mT field, by cooling through  $T_c$  at  $7 \mu\text{K}/\text{min}$  and 0.6 rad/s. Cooling was continued until  $0.81 T_c$ , where  $\Omega$  was slowly increased to 1.4 rad/s, to create the DQV lines. The final step was a slow deceleration to zero, during which the radial distributions  $N_1(r^2)$  and  $N_2(r^2)$  were recorded. Both  $\Omega$  sweeps were performed at  $|d\Omega/dt| = 2 \cdot 10^{-3}$  rad/s $^2$ . The critical CF velocity of vortex formation at 1.4 rad/s was  $\Omega_c = 0.24$  rad/s, which corresponds to a linear velocity of  $v_c = 0.60$  mm/s. The *inset* illustrates schematically the array configuration, a plastically deformed agglomerate of vortex lines.

SQV and DQV lines. These can be prepared by making use of the metastability of existing vorticity.

We use the following procedure: The sample is first cooled through  $T_c$  at  $\Omega \leq 0.6$  rad/s and  $H > H_c$ , so that an equilibrium vortex state with only SQV lines is formed. DQV lines are added later, by increasing  $\Omega$  slowly while the temperature is already below  $T_c$ , such that the desired number of DQV lines is created at a stable critical counterflow velocity  $v_c = \Omega_c R$  [1]. In the presence of an existing array this value of CF represents the separation between the annihilation and critical velocity thresholds. The DQV lines are here injected one at a time into the existing array, presumably from the same nucleation center on the cylindrical wall where the superflow instability takes place (i.e. they are thought to emanate from a rectilinear source which is close to the cylindrical wall and parallel to the rotation axis [1]).

In Fig. 14 the radial decomposition of an array is shown which has been prepared with this procedure, by adding 150 DQV lines to an existing equilibrium array of 310 SQV lines. During deceleration, initially both types of vortices are seen to annihilate, but on moving closer to the center the proportion of DQV lines is reduced and the SQV lines start to dominate. Such an annihilation record

could correspond to the configuration shown schematically in the inset of Fig. 14, which in turn could result from the process by which the array was formed. The DQV lines are here formed in a regular periodic process, where a newly created DQV line arrives roughly to the same spot at the edge of the array. It makes space for itself by pushing the existing lines aside. In this way the DQV lines end up residing in a segregated pocket at the edge of the cluster, if no mixing of lines occurs later.

From the data in Fig. 14 it is not possible to judge how sharp the boundary is between the two domains and to what extent mixing of the two vortex species might have occurred. However, no significant change from this configuration is noticed even if the cluster is subjected to rapid modulation of the rotation velocity with an amplitude which does not yet add new vortices or annihilate existing ones. On this basis we expect spontaneous reordering or annealing not to be of importance. The sequentially formed array is most likely a state with much reduced long-range order, which resembles a random glassy agglomerate, but is subject to hexagonal nearest-neighbor coordination and a circular boundary condition.

#### D. Homogeneity of superfluid transition

In Chap. V we have focused on two questions: (1) the metastability and width of the SQV  $\leftrightarrow$  DQV transition and (2) the configuration of the vortex array in the coexistence regime. We might now simply conclude that the segregated coaxial array, which is observed after a cool down through  $T_c$  in the coexistence regimes, is the expected minimum energy configuration. Since vortex clusters in  $^3\text{He-A}$  cannot relax during the course of the experiments, this configuration must also be the one which was originally formed in the transition through  $T_c$ .

However, in any real experiment the superfluid transition will acquire some degree of inhomogeneity. On some level this will lead to irreversibility and will interfere with the argument that the transition is adiabatic and minimizes the total energy. Here the main source for inhomogeneity is the thermal resistance concentrated in the orifice of the container. The liquid  $^3\text{He}$  volume consists of the sample container and the sintered heat exchanger in contact with the refrigerator. These are connected together with a long tube, which ends in the orifice on the bottom of the sample cylinder [18]. During cool down a thermal gradient is present, in addition to residual heat leaks, which maintain the top end of the sample container as the warmest point in the  $^3\text{He}$  column. This means that the heat flow through the orifice is composed of the cooling rate of the liquid and the residual heat leak. The residual heating consists of the NMR absorption and of thermal relaxation losses seeping out of the walls of the sample container.

At a cooling rate of  $1 \mu\text{K}/\text{min}$  the heat flow from the container is of order  $0.5 \text{ nW}$  and the thermal gradient inside the container  $\sim 0.5 \mu\text{K}/\text{mm}$  (at  $T_c \sim 2.4 \text{ mK}$ ). The superfluid transition emerges thus as a transition front through the orifice on the bottom of the cylinder. Initially it adopts a hemispherical shape [9]. The width of the phase front is determined by the local thermal gradient and thermal fluctuations. Its velocity can be controlled externally by adjusting the cooling rate. The heat flow, in turn, is mainly carried by a superfluid thermal countercurrent, which appears below  $T_c$  and converges towards the orifice. It is oriented predominantly in the axial direction, transverse to the rotational flow.

Clearly this picture of the transition is not that of a homogeneous second order transition (although it is probably closer to it than in any other macroscopic system). In equilibrium conditions at low  $\Omega$  the SQV is the minimum energy vortex structure, but thermal CF or other inhomogeneities provide a bias for DQV lines to be formed. This perturbation is concentrated in the neighborhood of the orifice, from where vortex formation starts during the superfluid transition. Here DQV lines are created first and SQV lines appear later when the transition front expands into the more homogeneous peripheral region of the cylinder. This interpretation, which is suggested by the dependence of the coexistence regime on the cooling rate at  $T_c$  (Fig. 12), provides a second reason for the coaxial array configuration with the SQV lines in the outer annulus.

According to this interpretation, the interface between the two coaxial domains becomes a similar phase boundary as that in Fig. 12, but now as a function of the radial coordinate  $r$  of the container, along which the cooling rate varies as the normal-to-superfluid phase front moves through the cylinder. This alternative explanation thus rests on the assumption that the cooling rate at  $T_c$  is one of the major controlling factors of the phase boundary in Fig. 12: SQV lines are formed closer to equilibrium conditions while nonequilibrium and perturbations favor the formation of DQV lines.

## VI. CONCLUSION

By comparing experiment to numerical simulation, we conclude that below  $T_c$  in superfluid  $^3\text{He}$  vortex arrays are formed by plastic deformation: Vortex lines are frozen in the array to the configuration in which the array was formed. High energy barriers separate different array configurations and thermally activated processes (or any other mechanisms) are not able to anneal faults, to create a new structure with lower energy and improved long range order.

In arrays formed by cooling through  $T_c$  in rotation, a segregated coaxial configuration is observed, with the SQV lines located in the outer annulus. Our numerical

analysis of 2D arrays with discrete rectilinear vortex lines confirms that this coaxial configuration is energetically the most preferable state in the coexistence regime. It is distinguished from all other segregated domain structures by a gain in the outer surface energy. This energy reduction arises on the scale of the intervortex distance rather than the container dimensions, due to a smoother outer interface, when the border is formed by vortex lines with a smaller quantum number.

### ACKNOWLEDGMENTS

This work was funded by the EU Human Capital and Mobility Programme (grants CHGECT94-0069 and ERBFMGECT980122) and by INTAS (grant 96-0610). NBK acknowledges support from the Russian Foundation for Basic Research (grant 99-02-16043).

- 
- [1] V. Ruutu, J. Kopu, M. Krusius, Ü. Parts, B. Plaçais, E. Thuneberg, and W. Xu, Phys. Rev. Lett. **79**, 5058 (1997).
- [2] Ü. Parts, J.M. Karimäki, J.H. Koivuniemi, M. Krusius, V.M. Ruutu, E.V. Thuneberg, and G.E. Volovik, Phys. Rev. Lett. **75**, 3320 (1995).
- [3] D.H.E. Dubin and T.M. O'Neil, Rev. Mod. Phys. **71**, 87 (1999).
- [4] D. Vollhardt and P. Wölfle, *The Superfluid Phases of Helium 3* (Taylor & Francis, London, 1990).
- [5] H.K. Seppälä, P.J. Hakonen, M. Krusius, T. Ohmi, M.M. Salomaa, J.T. Simola, and G.E. Volovik, Phys. Rev. Lett. **52**, 1802 (1984).
- [6] J.M. Karimäki and E.V. Thuneberg, Physica B **194-196**, 777 (1994); Phys. Rev. B **60**, 15290 (1999).
- [7] A.L. Fetter, in *Progress in Low Temperature Physics*, ed. D.F. Brewer (North-Holland, Amsterdam, 1986), Vol. 10, p. 1; M.M. Salomaa, and G.E. Volovik, Rev. Mod. Phys. **59**, 533 (1987).
- [8] H.K. Seppälä and G.E. Volovik, J. Low Temp. Phys. **51**, 279 (1983); V.Z. Vulovic, D.L. Stein, and A.L. Fetter, Phys. Rev. B **29**, 6090 (1984).
- [9] M. Krusius, E.V. Thuneberg, and Ü. Parts, Physica B **197**, 376 (1994).
- [10] L.J. Campbell and R.M. Ziff, Phys. Rev. B **20**, 1886 (1979).
- [11] In this report the so-called *dipole-unlocked soft core* in <sup>3</sup>He-A is referred to as the vortex core. Within the soft core the orientations of the spin  $\hat{\mathbf{d}}(\mathbf{r})$  and orbital  $\hat{\ell}(\mathbf{r})$  vector fields are unrelated (dipole unlocked), while outside in the bulk liquid  $\hat{\mathbf{d}}(\mathbf{r}) \parallel \hat{\ell}(\mathbf{r})$  (dipole locked). The dipole-unlocked soft core is formed when the external magnetic field  $H$  exceeds the equivalent of the dipolar spin-orbit coupling:  $H > H_D \sim 1$  mT. The radius of the soft core is proportional to  $\xi_D(T, P) \geq 8 \mu\text{m}$ , the temperature and pressure dependent dipolar healing length. It gives the length scale on which the order-parameter texture relaxes from dipole unlocked within the soft core to dipole locked outside in the bulk liquid. Within the soft core of a DQV line the orientations of the orbital unit vector  $\hat{\ell}$  extend over a solid angle of  $4\pi$  while in the case of the SQV line this angular distribution is over  $2\pi$  [6]. The soft core of the SQV includes a central *singular hard vortex core* with a diameter comparable to the superfluid coherence length  $\xi(T, P) \geq 10$  nm. It is the singular core which is responsible for the large critical velocity of the SQV line [1]. Thus the SQV and DQV structures differ not only in the topology of their  $\hat{\ell}$  fields.
- [12] I. M. Khalatnikov, *An Introduction to The Theory of Superfluidity* (W.A. Benjamin Inc., New York, 1965).
- [13] T.D. Bevan, A.J. Manninen, J.B. Cook, H. Alles, J.R. Hook, and H.E. Hall, J. Low Temp. Phys. **109**, 423 (1997); Phys. Rev. Lett. **77**, 5086 (1996).
- [14] V.V. Avilov, Solid State Commun. **44**, 555 (1982).
- [15] R.W. Hasse and V.V. Avilov, Phys. Rev. B **44**, 4506 (1991).
- [16] V.M. Ruutu, Ü. Parts, and M. Krusius, J. Low Temp. Phys. **103**, 1 (1996).
- [17] V.M. Ruutu, J.J. Ruohio, M. Krusius, B. Plaçais, E.B. Sonin, and W. Xu, Phys. Rev. B **56**, 14089 (1997-I); Physica B **255**, 27 (1998).
- [18] V.M. Ruutu, Ü. Parts, J.H. Koivuniemi, N.B. Kopnin, and M. Krusius, J. Low Temp. Phys. **107**, 93 (1997).
- [19] J.P. Pekola, K. Torizuka, A.J. Manninen, J.M. Kynnäräinen, and G.E. Volovik, Phys. Rev. Lett. **65**, 3293 (1990).